Effect of nanostructured electrode architecture and semiconductor deposition strategy on the photovoltaic performance of quantum dot sensitized solar cells

Mahmoud Samadpour[a,b], Sixto Giménez[a,*], Pablo P. Boix[a], Qing Shen[c,d], Mauricio E. Calvo[e], Nima Taghavinia[b,f], Azam Iraji zad[b,f], Taro Toyoda[c], Hernán Míguez[e], Iván Mora-Seró[a,*]

[a] Grup de Dispositius Fotovoltaics i Optoelectrònics, Departament de Física, Universitat Jaume I, 12071 Castelló, Spain
[b] Institute for Nanoscience and Nanotechnology, Sharif University of Technology, PO Box 11155-8639, Tehran, Iran
[c] Department of Engineering Science, Faculty of Informatics and Engineering, The University of Electro-Communications, 1-5-1 Chofugaoka, Chofu, Tokyo 182-8585, Japan
[d] PRESTO, Japan Science and Technology Agency (JST), 4-1-8 Honcho Kawaguchi, Saitama 332-0012, Japan
[e] Instituto de Ciencia de Materiales de Sevilla, CSIC-US, Avenida Américo Vespucio 49, 41092 Sevilla, Spain
[f] Department of Physics, Sharif University of Technology, PO Box 11155-9161, Tehran, Iran

ARTICLE INFO

ABSTRACT

Here we analyze the effect of two relevant aspects related to cell preparation on quantum dot sensitized solar cells (QDSCs) performance: the architecture of the TiO$_2$ nanostructured electrode and the growth method of quantum dots (QD). Particular attention is given to the effect on the photovoltage, V_{oc}, since this parameter conveys the main current limitation of QDSCs. We have analyzed electrodes directly sensitized with CdSe QDs grown by chemical bath deposition (CBD) and successive ionic layer adsorption and reaction (SILAR). We have carried out a systematic study comprising structural, optical, photophysical and photoelectrochemical characterization in order to correlate the material properties of the photoanodes with the functional performance of the manufactured QDSCs. The results show that the correspondence between photovoltaic conversion efficiency and the surface area of TiO$_2$ depends on the QDs deposition method. Higher V_{oc} values are systematically obtained for TiO$_2$ morphologies with decreasing surface area and for cells using CBD growth method. This is systematically correlated to a higher recombination resistance of CBD sensitized electrodes. Electron injection kinetics from QDs into TiO$_2$ also depends on both the TiO$_2$ structure and the QDs deposition method, being systematically faster for CBD. Only for electrodes prepared with small TiO$_2$ nanoparticles SILAR method presents better performance than CBD, indicating that the small pore size disturb the CBD growth method. These results have important implications for the optimization of QDSCs.

© 2012 Elsevier Ltd. All rights reserved.

1. Introduction

Considerable efforts have been made in the last years in order to push up the energy conversion efficiencies of quantum dot solar cells by using identical strategies previously developed for dye sensitized solar cells (DSCs). This approach has been successful as long as the efficiencies of QDSCs were around 1–2%. At present, the state-of-the-art efficiencies of QDSCs surpass 5% and the latest insights into the relevant processes for solar cell operation indicate that a whole redesign of the QDSCs concept is convenient in order to achieve higher efficiencies. The current record efficiencies of semiconductor-sensitized solar cells (SSCs) under full 1 sun illumination lays above 6%. This makes inorganic semiconductor materials a promising alternative to molecular sensitizers. Perovskite (CH$_3$NH$_3$)PbI$_3$ quantum dots (QDs), stable in I$^-$-I$_3^-$ redox

electrolyte, have reached 6.54% efficiency [1] while chalcogenide QD sensitized solar cells (QDSCs), stable in polysulfide electrolyte, showed 5.4% efficiency [2]. The efficiencies of sensitized solar cells, using a liquid hole conductor, remain lower compared to their counterparts using molecular dye sensitizers (DSCs) with 12% efficiency [3]. However, a faster progress in developing QDSCs has been obtained in the last years compared to DSCs. Regarding all-solid-state devices, the existing gap between QDSCs and DSCs has been bridged, as efficiencies around 6% have been reported for both kind of devices, using QDs or molecular dyes as sensitizers [4,5]. Again, since QDSCs are not fully optimized, it is expected that the efficiency of these devices will increase in the near future [6–11].

Many aspects in QDSCs remain under intense research in order to develop more efficient devices. From our point of view, the topics which must be studied in more detail for QDSC optimization are: (i) the architecture of the nanostructured photoanode; (ii) the QD preparation method; (iii) the hole transporting media [5,7,12]; (iv) the counter electrode material, particularly for liquid QDSCs using polysulfide electrolytes [13–17] and (v) the recombination process

* Corresponding authors.
E-mail addresses: sjulia@fca.uji.es (S. Giménez), sero@fca.uji.es (I. Mora-Seró).

[18–21]. In the present study, we focus on the two first issues. We evaluate the effect of both the architecture of the wide bandgap oxide semiconductor TiO$_2$ and the light absorbing semiconductor deposition strategy on the photovoltaic performance of QDSCs. We have paid special attention to the effect of both issues on the device photovoltage, V_{oc}, since this parameter conveys the main current limitation of QDSCs. Current V_{oc} values for QDSCs lay significantly below those reported for DSCs [22], while photocurrents, J_{sc}, as high as 18.4 mA/cm^2 [16], and fill factors, FF, higher than 0.62, have been reported for QDSCs [23], which are close to the values reported for high efficient DSCs.

One of the key points responsible for the high performance obtained with DSCs is the nanostructured electrodes. A monolayer of light absorbing molecular dye can only absorb a small quantity of the incident light. However, the use of nanostructured electrodes allows a factor 100–1000 increase of the effective surface area, and consequently, a similar increase of the optical density, or even higher if for example a light scattering layer is employed. When light absorbing materials with different properties are used (for example semiconductor QDs), the most suitable electrode structure leading to optimal functionality has to be found for several reasons. The smallest TiO$_2$ nanoparticles (around 10–15 nm), which are desired for high effective surface area, lead to the formation of 5–10 nm pores, leading to serious difficulties for QD loading and penetration of the electrolyte, which are deleterious for sensitized solar cell performance [19]. In addition, the much higher molar extinction coefficient of semiconductor QDs compared to molecular dyes, lead to a relaxation of the requirements related to the surface area of the mesoporous electrode in QDSCs [24]. In fact, high performing QDSCs, have been reported with alternative low surface area morphologies like TiO$_2$ inverse opals [25], Si–ZnO hierarchical pine-tree structures [22], or ZnO nanowires [22,26,27]. It is particularly relevant, the high V_{oc}, up to 0.77 V, values obtained with ZnO nanowires [22].

Another significant difference between semiconductor QDs and molecular dyes is the strong dependence of QD properties, and consequently solar cell performance, on the QD growth method and the attaching mode to the wide bandgap nanostructured semiconductor [21,28–32]. There are two main approaches for QD sensitization: (i) to use previously synthesized colloidal QDs [13,29,30] and (ii) to directly grow the QD on the surface of the wide bandgap semiconductor [12,19,20,23,33]. The direct growth of semiconductor QDs on the surface of the nanostructured electrode does not allow a fine control of the QDs properties, but produces a significant higher QD loading, increasing the solar cell photocurrent. In fact the highest efficiencies reported for QDSCs have been reported using a direct growth method [1,5,23].

Taking into account these considerations, in the present study we have analyzed nanostructured electrodes with different architectures directly sensitized with CdSe QDs grown by chemical bath deposition (CBD) [23,34] and successive ionic layer adsorption and reaction (SILAR) [12]. Both methods are based on low cost solution processes, ideal for up-scaling and fabrication of cost-effective photovoltaic devices. We have carried out a systematic study comprising structural, optical, photophysical and photoelectrochemical characterization in order to correlate the material properties of the photoanodes with the functional performance of the manufactured QDSCs. Particular attention is given to the correspondence between V_{oc} and both the electrode structure and QD growth method.

2. Experimental

2.1. Synthesis of the TiO$_2$ structures

Six different TiO$_2$ morphological structures were tested. Three structures were based on nanoparticles (P20, P250 and P20–450),

two on hollow fibers (F and F+P20) and one on inverse opal structures (O). The three nanoparticulated structures (P20, P250 and P20–450) were obtained from commercial pastes from Dyesol: DSL-18NR-T (TiO$_2$ particle size 20 nm), WER 2-O (TiO$_2$ particle size 250 nm) and DSL-18NR-AO (TiO$_2$ particle size 20–450 nm), respectively. The first paste produces electrodes with high effective surface area, while the other two are commonly employed as light scattering layers in DSCs. The hollow fibers (F) were synthesized as previously described [35,36]. A solution of ethyl cellulose solution was prepared by dissolving 1 g of ethyl cellulose in 12.5 ml ethanol assisted by ultrasonication. The paste for doctor blading was prepared by milling 0.2 g hollow fibers and 1 ml of the prepared solution of ethyl cellulose in ethanol in a mortar for 30 min while 1 ml of terpineol was added dropwise during the milling process. The F+P20 structure was prepared by mixing 60 wt% of the P20 paste with 40 wt% of the F paste.

Finally the inverse opals were prepared by infiltration of a three dimensional photonic colloidal crystal made of polystyrene spheres of 300 nm and 400 nm diameter. Spheres were deposited by spin coating, self-assembling on the substrate [37]. Next, a 2% methanolic TiCl$_4$ solution was added onto the self-assembled polystyrene spheres and samples were stored during 30 min at 80 °C. This process was repeated three times. After that, a thermal treatment (450 °C, 1 h, ramp: 1 °/min) was applied to remove the ordered polysterene template and to consolidate the TiO$_2$ inverse opal structure.

All the photoanodes (with the only exception of the O material) were doctor-bladed on transparent conducting fluorine doped tin oxide (FTO) glass substrates (sheet resistance ~10 Ω/□). The resulting photoelectrodes were sintered at 450 °C, to obtain good mechanical and electrical contact at the interfaces TiO$_2$/TiO$_2$ and TiO$_2$/substrate. Before deposition of the different TiO$_2$ structures, the FTO substrates were coated by a compact layer of TiO$_2$ deposited by spray pyrolysis (~100 nm thick). These electrodes were calcinated at 450 °C for 30 min. For samples O and F, it has been detected a low mechanical stability and poor adhesion with the substrate.

2.2. Electrode sensitization

The different TiO$_2$ nanostructured electrodes were sensitized by CdS/CdSe QDs directly grown on the photoelectrode surface. CdS was grown by 4 SILAR cycles. Cd^{2+} ions have been deposited from an ethanolic 0.05 M solution of Cd(NO$_3$)$_2$ × 4H$_2$O. The sulfide source was a 0.05 M solution of Na$_2$S × 9 H$_2$O in methanol/water (50/50, v/v) [33,38]. A single CdS SILAR cycle consisted of 1 min dip-coating of the TiO$_2$ working electrode into the metal precursors and subsequently into the sulfide solutions. After each bath, the photoanode is thoroughly rinsed by immersion in the corresponding solvent to remove the chemical residuals from the surface and subsequently dried in air. The CdSe deposition after CdS coating was performed by two methods SILAR and CBD. The SILAR process was carried out following the method developed before [12]. Briefly, 0.03 M Cd(NO$_3$)$_2$ in ethanol was used as the Cd^{2+} source and the in situ prepared 0.03 M Se^{2-} in ethanol was used as Se^{2-} precursor. Se^{2-} precursor is obtained from the reduction of SeO$_2$ by NaBH$_4$ in ethanol, see reference [12] for more details. For sensitization, the electrodes were successively dipped in these solutions inside a glove box under N$_2$ atmosphere. One SILAR cycle for CdSe consisted of 30 s dipping the TiO$_2$ working electrode into the Cd^{2+} precursor and subsequently into the selenide solution, during 30 s. After each bath, the photoanode was rinsed by immersion in pure ethanol to remove the chemical residuals from the surface and subsequently dried with a N$_2$ gun [19]. In the present study, 6 CdSe SILAR cycles have been performed for all the electrodes prepared with this process. The CBD process was carried out as previously described [21]: 80 mM
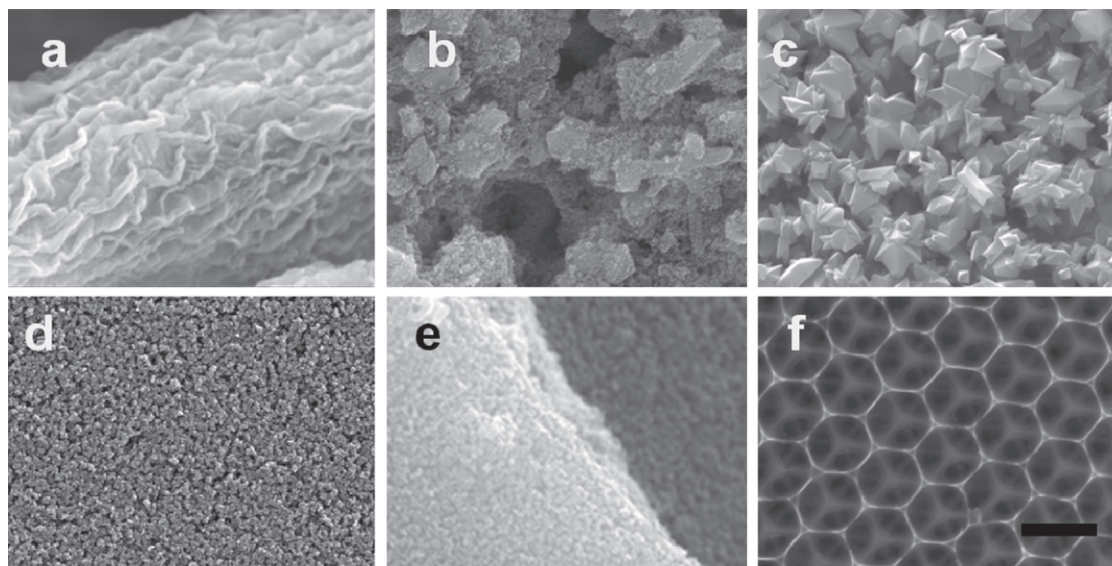
Fig. 1. Top view micrographs of the different tested TiO$_2$ structures. (a) F, (b) P20–450, (c) P250, (d) P20, (e) F + P20 and (f) O. The scale bar is 500 nm for all micrographs.

of sodium selenosulphate (Na$_2$SeSO$_3$) solution was prepared by refluxing elemental Se and Na$_2$SO$_3$ in Milli-Q water at 80 °C for 6 h with N$_2$ flux. The chemical bath solution was prepared by mixing 80 mM of CdSO$_4$ and 80 mM of Na$_2$SeSO$_3$ solution with 120 mM of nitriloacetic acid. The sensitized TiO$_2$ electrodes were immersed in the chemical bath solution at 10 °C for 12 h. Then, the electrodes were washed with Milli-Q water and dried with N$_2$ gun. It is well known that a seed layer of CdS significantly enhances the growth rate of CdSe, producing an increase of the light absorption for the same CBD deposition time. In order to improve the stability and performance of all SILAR and CBD electrodes, they were covered with a ZnS protective coating [19,39–41], by twice dipping alternatively into 0.1 M Zn(CH$_3$COO)$_2$ and 0.1 M Na$_2$S solutions for 1 min/dip, rinsing with Milli-Q ultrapure water between dips [41]. At least two cells with the same conditions (TiO$_2$ nanostructure and QD deposition mode) have been prepared and analyzed.

2.3. QDSC preparation

The solar cells were prepared by sandwiching a Cu$_2$S counter electrode and a QD-sensitized photoelectrode using a scotch tape spacer (thickness 50 μm) and permeating with polysulfide electrolyte. Polysulfide electrolyte contained 1 M Na$_2$S, 1 M S, and 0.1 M NaOH solution in Milli-Q ultrapure water [13,14]. The Cu$_2$S counter electrodes were prepared by immersing a brass foil in HCl solution at 70 °C for 5 min and subsequently dipping it into polysulfide solution for 10 min, resulting in a porous Cu$_2$S electrode. The geometric area of the cells was 0.28 cm^2.

2.4. Photoanode and solar cell characterization

Gas adsorption measurements, BET, were performed on a Micromeritics ASAP 2020 surface area and porosity analyzer with the ASAP 2020 V3.04 E software. Three measurements were carried out for each specimen in order to assess the reproducibility of the results. Microstructural examination of the sensitized photoanodes was carried out by a JSM-7000F JEOL FEG-SEM system (Tokyo, Japan). Transmission electron microscopy was carried out by using a high resolution TEM (HRTEM) Field Emission Gun JEM-2100 electron microscope (JEOL) operated at 200 kV. TEM samples were prepared by raking off the mesoporous sensitized photoanodes from the FTO coated glass. The powder specimens were sonicated

in absolute ethanol for 5 min, and a few drops of the resulting suspension were deposited onto a holey-carbon film supported on a copper grid, which was subsequently dried.

The optical absorption spectra of the photoanodes were recorded in the range of 300–800 nm by a Cary 500 UV-VIS Varian spectrometer, no integrating sphere has been employed in the measurement. Current–potential (J–V) curves, impedance spectroscopy (IS) measurement, applied bias voltage decay (ABVD) [42] were carried out with a FRA equipped PGSTAT-30 potentiostat from Autolab. J–V measurements were carried out using mask (0.24 cm^2). Cells were illuminated using a solar simulator at AM1.5 G, where the light intensity was adjusted with an NREL calibrated Si solar cell with a KG-5 filter to one sun intensity (100 mW/cm^2). Incident photon to electron conversion efficiency (IPCE) measurements have been performed employing a 150 W Xe lamp coupled with a computer-controlled monochromator. The photocurrent was measured using a nanoammeter 70310 from Oriel Instruments. Impedance spectroscopy measurements were carried out in dark conditions applying a 20 mV AC signal with the frequency ranging between 400 kHz and 0.1 Hz at different forward biases. Ultrafast carrier dynamics have been evaluated by the lens-free heterodyne detection transient grating (LF-HD-TG) technique. The principles and experimental setup of the technique have been described before [43–46]. In the present study, the laser source was a titanium/sapphire laser (CPA-2010, Clark-MXR Inc.) with a wavelength of 775 nm, a repetition rate of 1 kHz, and a pulse width of 150 fs. The light was separated into two parts. Half of it was used as a probe pulse. The other half of the light was used to pump an optical parametric amplifier (OPA) (a TOAPS from Quantronix) to generate light pulses with a wavelength tunable from 290 nm to 3 μm; used as a pump light in the TG measurement. In this study, the pump pulse wavelength was 520 nm and the probe pulse wavelength was 775 nm. Since most reliable results are obtained working in transmission configuration, only P20 and F specimens were tested.

3. Results and discussion

3.1. Structural characterization

The relationship between structural features and functional performance of the devices provides a powerful tool both to understand the mechanisms of the relevant processes taking place during
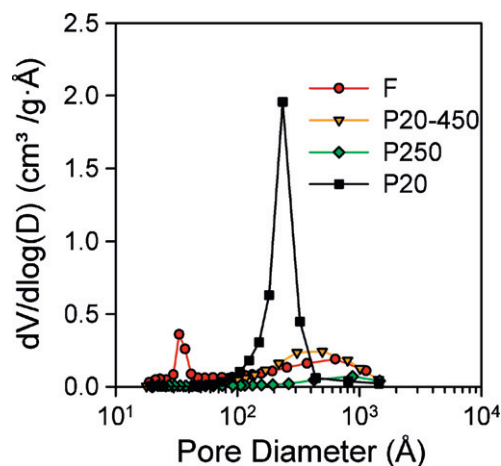
Fig. 2. Size distribution extracted from BET measurements for the different structures tested.

device operation as well as to optimize the design of the different components leading to optimum performance [10]. Fig. 1 shows the top view of the different TiO$_2$ structures studied. The cross sectional views are included in the Supplementary Information as Fig. SI1. From these micrographs, it is clear the different electrode morphology and the different size distribution of the nanoparticulated structures. In addition, BET measurements were used for the determination of the pore size. The P20 material is characterized by a narrow size distribution around 20 nm (see Fig. 2), and it is used as the typical structure for transparent TiO$_2$ electrodes. The other two nanoparticulated systems (P20–450 and P250) are used as scattering layers in DSCs, due to the bigger mean size of the particles. The P250 structure possesses a narrower size distribution than the previous ones around 250 nm, while the P20–450 structure comprises a wide size distribution ranging from 20 nm to 450 nm.

In spite of its micrometric size of F, its structure exhibits a nanoporous wall structure, peaking at about 2–3 nm as shown in Figs. 1(a) and 2 [36]. We will consider that this nanometric pore size is not suitable for the in situ deposition of QDs by SILAR or CBD, since the QD size is larger than these pores. In this aspect, the effective surface area of TiO$_2$ for QD deposition is lower compared to the surface area of TiO$_2$ obtained from BET measurements (Table 1). In the F + P20 structure, the hollow fibers appear to be glued by P20 nanoparticles as showed in Fig. 1(e), and consequently the adhesion of the hollow fibers to the FTO substrate is significantly improved in this hybrid fibrous-nanoparticulated structure. Finally, the O structure is highly porous and perfectly ordered with a characteristic void diameter of 400 nm, Fig. 1(f).

The surface area of some of these structures measured by BET together with the porosity calculated from the film morphology and geometrical dimensions are summarized in Table 1. With this information and taking into account the above considerations assumed for the hollow fibers, F, the different morphologies have been ranked in terms of their total active

Table 1
BET surface area, porosity and total area of the electrodes with the different TiO$_2$ structures (geometrical area of the electrodes is 0.24 cm^2).

TiO$_2$ morphology	BET (m^2/g)	Porosity	Total surface (cm^2)
F	82.84	0.90	268[a]
P20–450	27.33	0.29	250
P250	10.15	0.31	92
P20	73.82	0.40	675

[a] Surface area considering the 2–3 nm porosity, see Fig. 2, note that the surface available for QD deposition is sensibly lower as the QD size is larger than these nanometric pores.

area as: P20 > F + P20 > P20–450 > P250 > F > O. Upon sensitization by SILAR or CBD methods, the structure of the TiO$_2$ photoelectrodes in now conformally coated with a thin film of CdS/CdSe (thickness around 5 nm). These structures were measured by TEM and are shown in the Supplementary Material in Fig. SI2. From these TEM micrographs, no significant morphological changes in the QDs layer structure are observed between both deposition methods (CBD and SILAR).

3.2. Optoelectronic characterization

One of the key functional properties of the photoelectrodes is the light harvesting capability. Consequently, the optical absorbance of the sensitized electrodes is shown in Fig. 3. There is a good correlation between the absorbance and the surface area independently of the sensitization method (SILAR or CBD), indicating that QD loading is proportional to the TiO$_2$ effective surface area. Conversely, the correspondence of the measured IPCE (Fig. 3) with the surface area of the electrodes is dependent on the sensitization method. When SILAR is employed, the IPCE increases monotonically with the surface area of the electrodes (i.e. optical absorbance), while when CBD is used, this trend is not followed for the highest surface area structure (material T). The maximum IPCE values obtained in the present study are about 60–70%. The use of TiO$_2$ layers with different structures in the same electrode in order to improve the light scattering enhances the IPCE results obtained in this work [19,20,23,36], but are not in the scope of the present study. In this study we are interested in the effect of each particular structure on the QDSC performance.

Note that direct light absorption measurement, Fig. 3, not only takes into account the light absorption of the different materials of the sensitized electrode but also the effect of light scattering. As we work without integrated sphere we have removed the scattering effect subtracting the absorption of the electrode before sensitization. This procedure gives the tendency of the light absorption but not the exact values. Note that some absorption still present at long wavelengths indicates that the scattering effect is not totally removed. For that reason we have used arbitrary units instead of absorption units.

The J–V curves of these solar cells under 100 mW/cm^2 AM1.5 illumination are compiled in Fig. 4 and the extracted photovoltaic parameters are listed in Table 2. As expected, the correspondence between IPCE and surface area of the electrodes observed in Fig. 3 is mimicked by the short-circuit current. The values of the open circuit voltage present a significant variation depending on the nanostructured electrode and the QD growth method, laying between 0.5 and 0.65 V. V_{oc} systematically decreases with increasing surface with the exception of the structures O and F. These structures, however, exhibit low mechanical stability and poor adhesion with the substrate. This behavior is more clearly illustrated in Fig. 5, where the photovoltaic parameters are plotted for the different TiO$_2$ structures ranked by active surface area (O < F < P250 < P20–450 < F + P20 < P20) and for both QDs deposition methods, CBD and SILAR. The monotonic increase of J_{sc} with surface area observed for SILAR samples is systematically correlated to a concomitant decrease of V_{oc}. Furthermore, these trends are translated into a progressive increase of efficiency with surface area, balanced for the structure with the highest surface area (P20). On the other hand, for CBD, the increase of J_{sc} with surface area does not take place for the structures with highest surface area, while V_{oc} shows identical behavior compared to the SILAR counterpart. This leads to an efficiency peak at an intermediate surface area (P20–450 structure), and decreasing for the samples with highest surface area. The described trends have the following implications: the solar cell parameters strongly depend on both the architecture of the nanostructured electrode and the QD growth method.
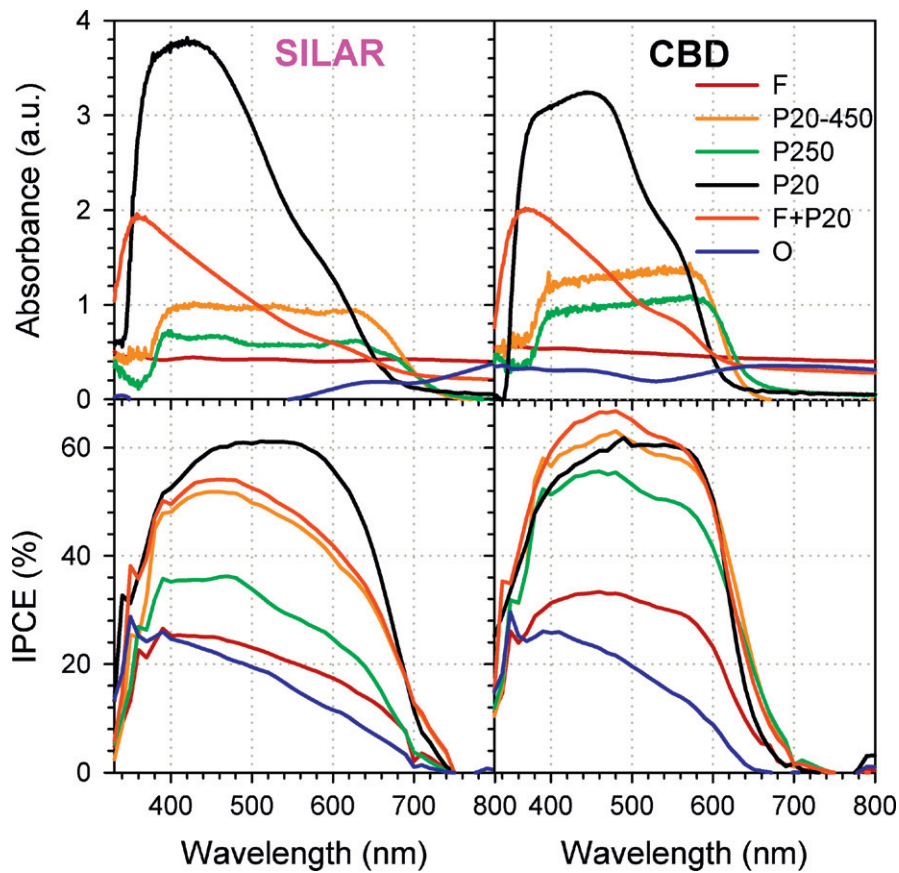
Fig. 3. Optical absorbance of the sensitized electrodes and IPCE of the respective manufactured solar cells.

Focusing on the effect on V_{oc}, we systematic observed higher V_{oc} values for CBD samples, see Fig. 6. Note, despite the poor adhesion of the studied O and F electrodes V_{oc} is also higher for CBD cells in this situation compared to SILAR samples. Open structures (i.e. lower effective surface area) also exhibit higher V_{oc} values. The SILAR method is more adequate for structures with high surface area. Conversely, the CBD method produces better performing devices for more opened structures, see Table 2. In the CBD method both precursors (Cd and Se) have to diffuse along the electrode pores in order to produce a uniform deposition, while only one precursor has to diffuse in the SILAR process. Probably the smallest pore size of P20 structure hinders the CBD process. In addition, the CBD process takes place at 10 °C, while the SILAR process takes place at room temperature.

Table 2
Photovoltaic parameters of the tested solar cells under 1 sun AM1.5G illumination.

	QD deposition	V_{oc} (V)	J_{sc} (mA/cm^2)	FF	η (%)
F	SILAR	0.51	2.33	0.47	0.56
F	CBD	0.60	2.56	0.46	0.72
P20–450	SILAR	0.56	6.98	0.52	2.05
P20–450	CBD	0.65	7.59	0.56	2.80
P250	SILAR	0.57	5.00	0.52	1.48
P250	CBD	0.64	5.45	0.58	2.04
P20	SILAR	0.50	9.86	0.46	2.28
P20	CBD	0.50	7.84	0.51	2.10
F + P20	SILAR	0.52	8.04	0.57	2.38
F + P20	CBD	0.60	7.33	0.58	2.57
O	SILAR	0.43	2.66	0.51	0.59
O	CBD	0.62	2.12	0.35	0.47

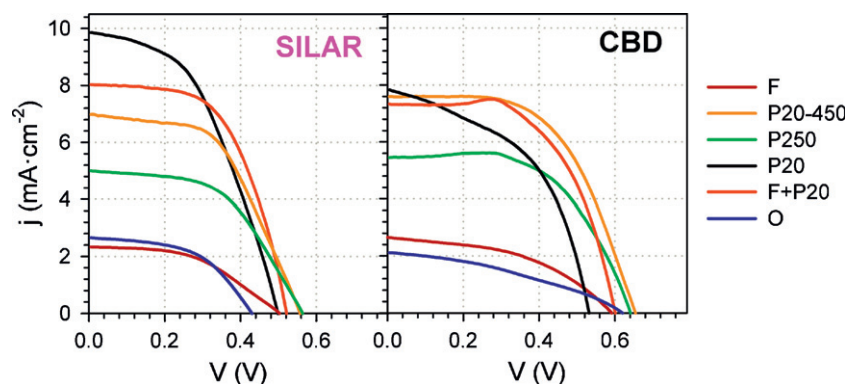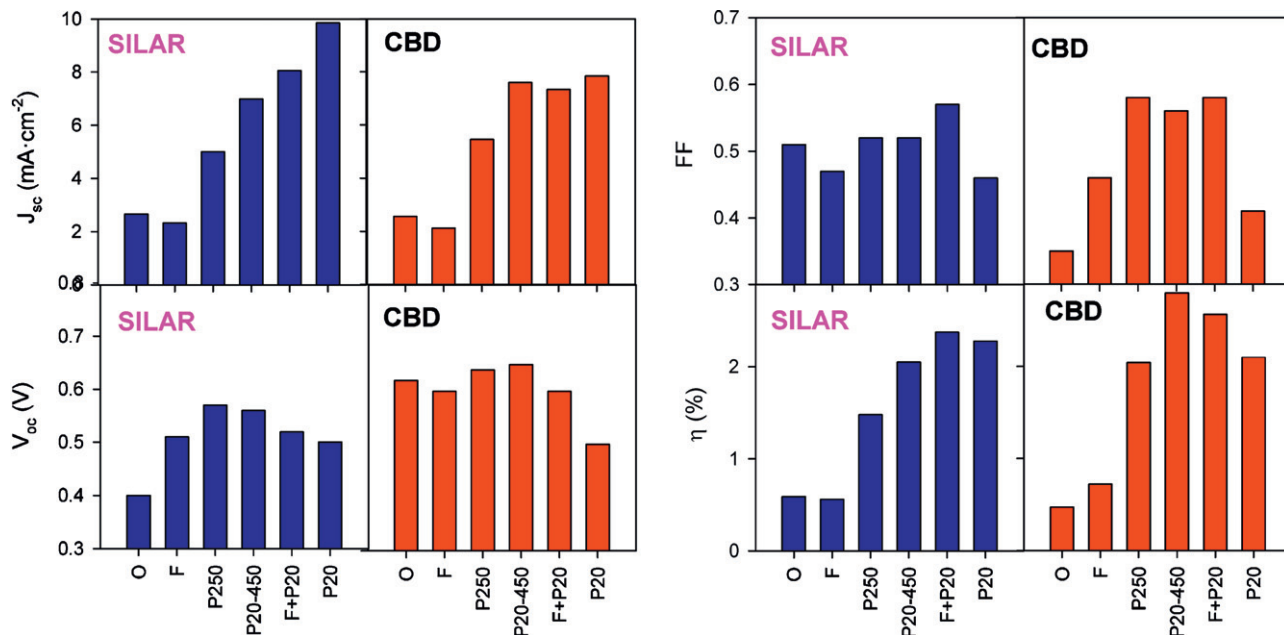**Fig. 4.** *J–V* curves of the different solar cells.

Fig. 5. Photovoltaic parameters for the different TiO_2 morphologies ranked by surface area (O < F < P250 < P20–450 < F + P20 < P20) for both QDs deposition methods, CBD and SILAR.

3.3. Impedance and ultrarapid characterization

In order to further understand the photoelectrochemical performance of the tested solar cells, impedance spectroscopy characterization in the dark was carried out and experimental data were fitted to the previously developed physical model for QDSCs [19–21,33]. The chemical capacitance, C_μ, shows a characteristic exponential behavior with the voltage drop at the sensitized TiO_2 (V_F), see Fig. 7, reflecting the exponential distribution of trap states near the conduction band edge [47,48]. V_F has been obtained from the applied bias, V_{appl}, removing the voltage drop in the series resistance, V_S, as $V_F = V_{appl} - V_S$ [48]. C_μ in Fig. 7 has been normalized to the TiO_2 volume taking into account the TiO_2 surface and thickness and the porosity extracted from BET measurements, for samples

P20, P20–450 and P250. This normalization allows a fair comparison between electrodes with different TiO_2 structure. As a general trend, it can be observed that the chemical capacitance for same structure does not vary with the QD growth method. This trend is also followed by the F + P20; F and O samples, see Fig. SI3. Conversely, the behavior of the P250 structure is an exception. Then, it can be concluded that the QD growth method does not affect the relative position of the TiO_2 conduction band. On the other hand, a shift in C_μ can be observed depending on the TiO_2 structure. Samples prepared with scattering pastes exhibit an upwards displacement of the conduction band, contributing to the higher V_{oc} obtained for P20–450 and P250 samples in comparison with P20 sample, see Table 2, note that comparing samples using the same deposition method, SILAR or CBD, P20–450 and P250 presents higher V_{oc} than P20 sample.

Fig. 8 shows the recombination resistance (R_{rec}) for the different tested samples, comparing cells with the same nanostructured electrode and different QD deposition method, CBD and SILAR. As a general trend, it can be observed that CBD specimens show higher recombination resistance (lower recombination rate) [48] compared to SILAR samples. The O structure is an exception, but the results obtained with this structure are less reproducible due
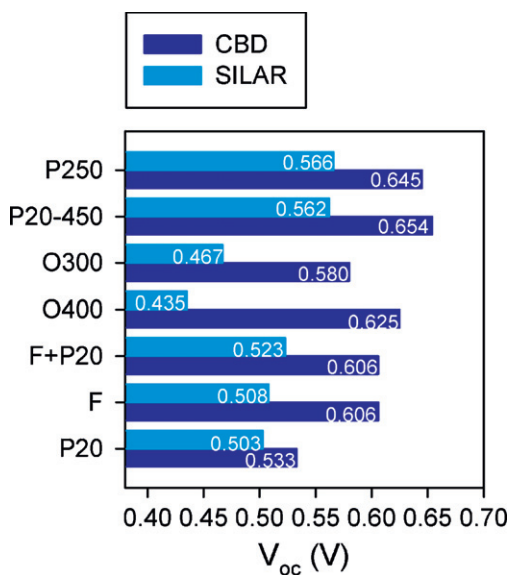

Fig. 6. V_{oc} values obtained for the different TiO_2 structures and for both QDs deposition methods, CBD and SILAR. O300 and O400 indicate the inverse opal pore size, 300 and 400 nm, respectively.
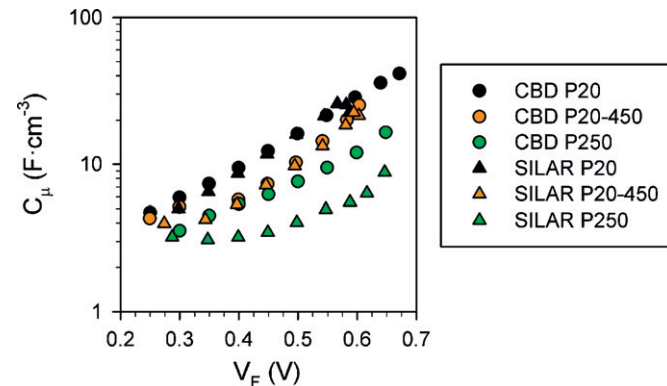

Fig. 7. Chemical capacitance of P20, P20–450 and P250 samples normalized to TiO_2 electrode volume comparing CBD and SILAR.
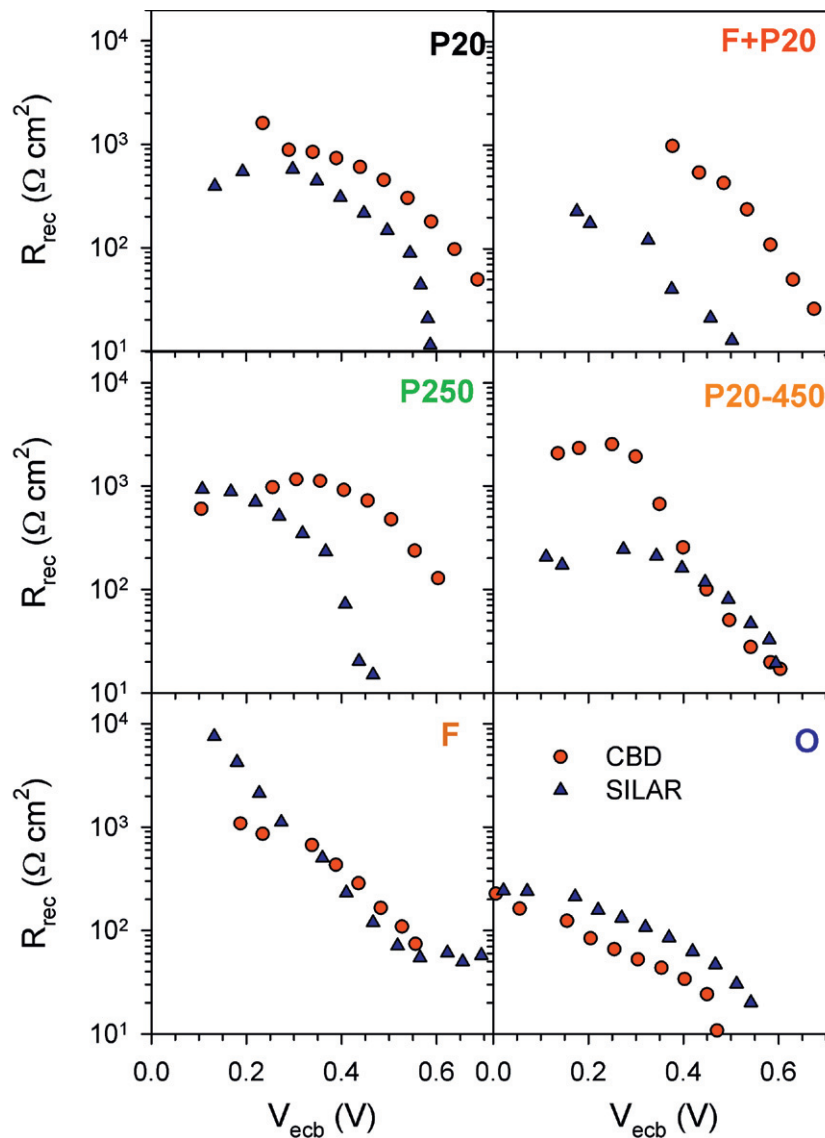
Fig. 8. R_{rec} for the different TiO$_2$ morphologies comparing CBD vs SILAR.

to mechanical adhesion problems, leading to difficulties for the direct comparison between different samples. This trend explains the higher V_{oc} detected in CBD cells. On the other hand, it has been shown that the QDs have an active role on the recombination process in QDSCs [32,39,49]. Consequently, from the point of view of recombination, the results presented in this study indicate that compared to SILAR grown QDs, the CBD growth method produces semiconductor QDs with enhanced properties.

Together with the recombination resistance, injection kinetics is a key property for the functional operation of solar cells. It has been shown that, excluding recombination effect, there is a direct correlation between photoinjection and cell performance [50]. Consequently, ultrafast carrier dynamics was characterized by the TG-LF-HD technique in order to evaluate the effect of the different TiO$_2$ morphologies and QDs sensitization method on the injection kinetics. In general, charge trapping and charge transfer processes can be studied as showed in the scheme of Fig. 9(a). As an example, Fig. 9(b) illustrates the TG response of the P20 sample sensitized with CdSe by SILAR. In this study, the pump light was changed from 2 mW to 10 mW and we have confirmed that there is no light intensity dependence for the TG kinetics under such experimental conditions. Recent studies [28] indicate that the

relaxation of the TG signal of TiO$_2$/CdSe nanocomposite structures can be fitted to a double exponential decay [32,39,50]:

$$Y = A_1 e^{-t/\tau_1} + A_2 e^{-t/\tau_2} \tag{1}$$

where A_1 and A_2 are preexponential factors and τ_1 (fast component) reflects the electron injection from QDs in intimate contact with the TiO$_2$ surface and the contribution of hole dynamics (provided that the ratio A_1/A_2 is close to 0.3), see Fig. 9(a) [32]. On the other hand, τ_2 (slow component) includes the contribution to the electron injection from QDs which are not in direct contact with TiO$_2$, see Fig. 9(a) [32]. The results of the fittings are shown in Table 3 for P20 and F structures with CdSe QDs deposited by both SILAR and CBD. For the P20 structure, the fast component, τ_1 is mainly related to the electron injection from QDs close to the surface although there is also contribution from hole dynamics ($A_1/A_2 \sim 0.6$). Conversely, the contribution of hole dynamics is negligible for the F material ($A_1/A_2 \sim 1.4$) and τ_1 totally reflects electron injection from QDs close to the surface. Both τ_1 and τ_2 are significantly shorter for the F material compared to P20, indicating faster kinetics of the fibrous structure. This can be due to the uncovered area of transparent conducting substrate (SnO$_2$:F) in the case of F sample. It has been shown that the QD injection from CdSe QDs into SnO$_2$ is faster

Table 3
Summary of the fitting parameters for the transient grating response of the P20 and F structures sensitized via both SILAR and CBD using a biexponential decay function.

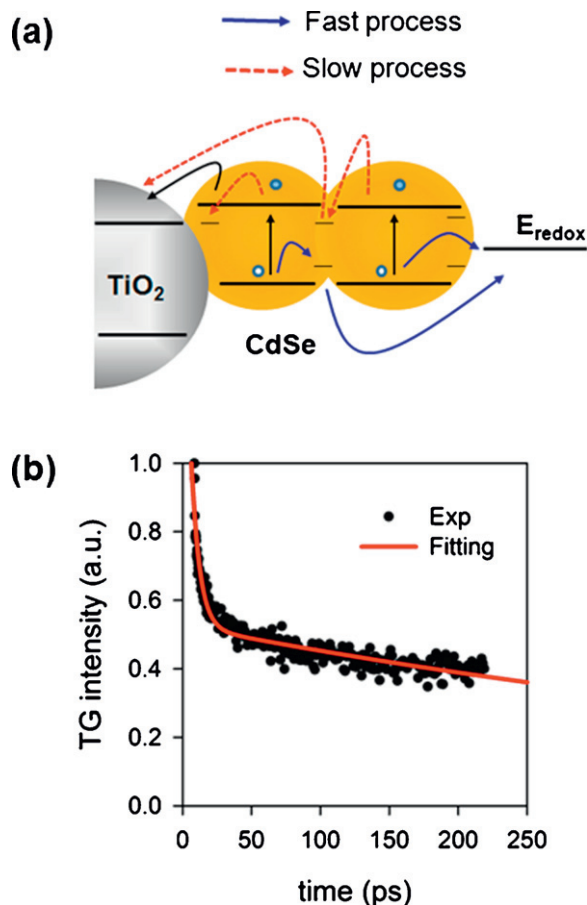| Sample		τ_1 (ps)	τ_2 (ps)	A_1	A_2
P20	SILAR	6.0 ± 0.4	660 ± 36	0.33 ± 0.01	0.52 ± 0.01
P20	CBD	6.6 ± 0.9	442 ± 38	0.34 ± 0.02	0.55 ± 0.01
F	SILAR	0.3 ± 0.1	12.9 ± 0.9	0.60 ± 0.07	0.42 ± 0.02
F	CBD	0.5 ± 0.1	4.9 ± 0.9	0.72 ± 0.08	0.33 ± 0.06

Fig. 9. (a) Scheme of the different charge trapping and charge transfer processes monitored by ultrafast carrier dynamics. (b) Characteristic experimental TG response of a P20 sample sensitized with CdSe grown by SILAR (dots) and the fitting to a biexponential decay (solid line).

than the injection into TiO$_2$ [51]. Comparing both QDs deposition methods, τ_2 is systematically shorter for CBD, indicating a clear difference between QD layers grown by CBD and SILAR. It has been observed that faster injection produces high performing cells [50]. The growth method has a strong influence on both the electron injection and the recombination process.

4. Conclusions

We demonstrated the key role of the TiO$_2$ structure and the QDs deposition method on the performance of QDSCs. The optical absorbance is directly proportional to the surface area of the electrodes. Conversely, the dependence of the photovoltaic conversion efficiency with the surface area of TiO$_2$ is different for both QDs deposition methods. SILAR is more adequate for high surface structures, where a monotonic increase of J_{sc} with surface area is obtained. The small pore size of high surface area structures and the lower growth temperature conditions hinder the growth of QDs by the CBD method, limiting the efficiency of these cells. The highest J_{sc}, when CBD is used, are obtained for intermediate surface areas, with enough QD loading and no diffusion limitation of the growth process. As a relevant result, higher V_{oc} values are systematically obtained with decreasing surface area TiO$_2$ morphologies and for the CBD method. This is systematically correlated to an upwards shift in the TiO$_2$ conduction band of scattering pastes with regard to transparent paste and to the higher recombination resistance (lower recombination rate) observed for CBD samples in comparison with SILAR cells. Injection kinetics is also dependent on both the TiO$_2$ structure and QDs deposition method, being systematically faster for CBD. The recombination and injection analysis indicate that CBD and SILAR growth methods produce CdSe QDs with significantly different properties from the point of view of photovoltaic conversion in sensitized devices. CBD leads to generally higher performing solar cells, with the already commented exception. These results have strong implications for the optimization of QDSCs performance.

Acknowledgements

Appendix A. Supplementary data

Supplementary data associated with this article can be found, in the online version, at http://dx.doi.org/10.1016/j.electacta.2012.04.087.

References

[1] J.-H. Im, C.-R. Lee, J.-W. Lee, S.-W. Park, N.-G. Park, Nanoscale 3 (2011) 4088.
[2] P.K. Santra, P.V. Kamat, Journal of the American Chemical Society 134 (2012) 2508.
[3] A. Yella, H.-W. Lee, H.N. Tsao, C. Yi, A.K. Chandiran, M.K. Nazeeruddin, E.W.-G. Diau, C.-Y. Yeh, S.M. Zakeeruddin, M. Grätzel, Science 334 (2011) 629.
[4] N. Cai, S.-J. Moon, L. Cevey-Ha, T. Moehl, R. Humphry-Baker, P. Wang, S.M. Zakeeruddin, M. Grätzel, Nano Letters 11 (2011) 1452.
[5] S.H. Im, C.-S. Lim, J.A. Chang, Y.H. Lee, N. Maiti, H.-J. Kim, M.K. Nazeeruddin, M. Grätzel, S.I. Seok, Nano Letters 11 (2011) 4789.
[6] F. Hetsch, X. Xu, H. Wang, S.V. Kershaw, A.L. Rogach, Journal of Physical Chemistry Letters 2 (2011) 1879.
[7] G. Hodes, Journal of Physical Chemistry C 112 (2008) 17778.
[8] P.V. Kamat, Journal of Physical Chemistry C 112 (2008) 18737.
[9] P.V. Kamat, K. Tvrdy, D.R. Baker, J.G. Radich, Chemical Reviews 110 (2010) 6664.
[10] I. Mora-Seró, J. Bisquert, Journal of Physical Chemistry Letters 1 (2011) 3046.
[11] S. Rühle, M. Shalom, A. Zaban, ChemPhysChem 11 (2010) 2290.
[12] H. Lee, M. Wang, P. Chen, D.R. Gamelin, S.M. Zakeeruddin, M. Grätzel, M.K. Nazeeruddin, Nano Letters 9 (2009) 4221.
[13] S. Giménez, I. Mora-Seró, L. Macor, N. Guijarro, T. Lana-Villarreal, R. Gómez, L.J. Diguna, Q. Shen, T. Toyoda, J. Bisquert, Nanotechnology 20 (2009).
[14] G. Hodes, J. Manassen, D. Cahen, Journal of the Electrochemical Society 127 (1980) 544.
[15] I. Mora-Seró, S. Giménez, T. Moehl, F. Fabregat-Santiago, T. Lana-Villareal, R. Gómez, J. Bisquert, Nanotechnology 19 (2008) 424007.
[16] J.G. Radich, R. Dwyer, P.V. Kamat, Journal of Physical Chemistry Letters 2 (2011) 2453.

[17] Z. Tachan, M. Shalom, I. Hod, S. Rühle, S. Tirosh, A. Zaban, Journal of Physical Chemistry C 115 (2011) 6162.
[18] E.M. Barea, M. Shalom, S. Giménez, I. Hod, I. Mora-Seró, A. Zaban, J. Bisquert, Journal of the American Chemical Society 132 (2010) 6834.
[19] V. González-Pedro, X. Xu, I. Mora-Seró, J. Bisquert, ACS Nano 4 (2010) 5783.
[20] M.A. Hossain, J.R. Jennings, Z.Y. Koh, Q. Wang, ACS Nano 5 (2011) 3172.
[21] I. Mora-Seró, S. Giménez, F. Fabregat-Santiago, R. Gómez, Q. Shen, T. Toyoda, J. Bisquert, Accounts of Chemical Research 42 (2009) 1848.
[22] P. Sudhagar, T. Song, D.H. Lee, I. Mora-Seró, J. Bisquert, M. Laudenslager, W.M. Sigmund, W.I. Park, U. Paik, Y.S. Kang, Journal of Physical Chemistry Letters 2 (2011) 1984.
[23] Q. Zhang, X. Guo, X. Huang, S. Huang, D. Li, Y. Luo, Q. Shen, T. Toyoda, Q. Meng, Physical Chemistry Chemical Physics 13 (2011) 4659.
[24] W.W. Yu, L. Qu, W. Guo, X. Peng, Chemistry of Materials 15 (2003) 2854.
[25] L.J. Diguna, Q. Shen, J. Kobayashi, T. Toyoda, Applied Physics Letters 91 (2007).
[26] A. Rogach, C. Luan, A. Vaneski, A. Susha, X. Xu, H.-E. Wang, X. Chen, W. Zhang, J. Xu, C.-S. Lee, J.A. Zapien, Nanoscale Research Letters 6 (2011) 340.
[27] M. Seol, H. Kim, Y. Tak, K. Yong, Chemical Communications 46 (2010) 5521.
[28] N. Guijarro, T. Lana-Villarreal, I. Mora-Seró, J. Bisquert, R. Gómez, Journal of Physical Chemistry C 113 (2009) 4208.
[29] I. Robel, V. Subramanian, M. Kuno, P.V. Kamat, Journal of the American Chemical Society 128 (2006) 2385.
[30] D.F. Watson, Journal of Physical Chemistry Letters 1 (2010) 2299.
[31] S. Giménez, X. Xu, T. Lana-Villarreal, R. Gómez, S. Agouram, Muñoz-Sanjosé, I. Mora-Seró, Journal of Applied Physics 108 (2010) 064310.
[32] N. Guijarro, T. Lana-Villarreal, Q. Shen, T. Toyoda, R. Gómez, Journal of Physical Chemistry C 114 (2010) 21928.
[33] A. Braga, S. Giménez, I. Concina, A. Vomiero, I. Mora-Seró, Journal of Physical Chemistry Letters 2 (2011) 454.
[34] O. Niitsoo, S.K. Sarkar, C. Pejoux, S. Rühle, D. Cahen, G. Hodes, Journal of Photochemistry and Photobiology A: Chemistry 181 (2006) 306.
[35] M.K. Aminian, N. Taghavinia, A. Iraji-Zad, S.M. Mahdavi, M. Chavoshi, S. Ahmadian, Nanotechnology 17 (2006) 520.
[36] M. Samadpour, S. Gimenez, A. Iraji Zad, N. Taghavinia, I. Mora-Sero, Physical Chemistry Chemical Physics 14 (2011) 522.
[37] A. Mihi, M. Ocaña, H. Míguez, Advanced Materials 18 (2006) 2244.
[38] H.J. Lee, H.C. Leventis, S.-J. Moon, P. Chen, S. Ito, S.A. Haque, T. Torres, F. Nüesch, T. Geiger, S.M. Zakeeruddin, M. Grätzel, M.K. Nazeeruddin, Advanced Functional Materials 19 (2009) 2735.
[39] N. Guijarro, J.M. Campiña, Q. Shen, T. Toyoda, T. Lana-Villarreal, R. Gómez, Physical Chemistry Chemical Physics 13 (2011) 12024.
[40] H.J. Lee, J. Bang, J. Park, S. Kim, S.M. Park, Chemistry of Materials 22 (2010) 5636.
[41] Q. Shen, J. Kobayashi, L.J. Diguna, T. Toyoda, Journal of Applied Physics 103 (2008).
[42] J. Bisquert, A. Zaban, M. Greenshtein, I. Mora-Seró, Journal of the American Chemical Society 126 (2004) 13550.
[43] L.J. Diguna, Q. Shen, A. Sato, K. Katayama, T. Sawada, T. Toyoda, Materials Science & Engineering C-Biomimetic and Supramolecular Systems 27 (2007) 1514.
[44] Q. Shen, M. Yanai, K. Katayama, T. Sawada, T. Toyoda, Chemical Physics Letters 442 (89) (2007).
[45] Q. Shen, K. Katayama, T. Sawada, M. Yamaguchi, T. Toyoda, Japanese Journal of Applied Physics Part 1-Regular Papers Brief Communications & Review Papers 45 (2006) 5569.
[46] M. Yamaguchi, K. Katayama, Q. Shen, T. Toyoda, T. Sawada, Chemical Physics Letters 427 (2006) 192.
[47] J. Bisquert, Physical Chemistry Chemical Physics 5 (2003) 5360.
[48] F. Fabregat-Santiago, G. Garcia-Belmonte, I. Mora-Seró, J. Bisquert, Physical Chemistry Chemical Physics 13 (2011) 9083.
[49] Hod, V. González-Pedro, Z. Tachan, F. Fabregat-Santiago, I. Mora-Seró, J. Bisquert, A. Zaban, Journal of Physical Chemistry Letters 2 (2011) 3032.
[50] N. Guijarro, Q. Shen, S. Giménez, I. Mora-Seró, J. Bisquert, T. Lana-Villarreal, T. Toyoda, R. Gómez, Journal of Physical Chemistry C 114 (22352) (2010).
[51] K. Tvrdy, P.A. Frantsuzov, P.V. Kamat, Proceedings of the National Academy of Sciences of the United States of America 108 (29) (2011).